Topological network transport in on-chip phononic crystals

Riyi Zheng,[1,*] Mou Yan,[2,*] Jien Wu,[1] Weiyin Deng,[1,†] Jiuyang Lu,[1,‡] Xueqin Huang,[1,§] and Zhengyou Liu[3,4,‖]

[1]*School of Physics and Optoelectronics and State Key Laboratory of Luminescent Materials and Devices, South China University of Technology, Guangzhou 510640, China*

[2]*School of Physics and Microelectronics, Key Laboratory of Materials Physics of Ministry of Education, Zhengzhou University, Zhengzhou 450001, China*

[3]*Key Laboratory of Artificial Micro- and Nanostructures of Ministry of Education and School of Physics and Technology, Wuhan University, Wuhan 430072, China*

[4]*Institute for Advanced Studies, Wuhan University, Wuhan 430072, China*

(Received 17 January 2023; revised 31 May 2023; accepted 1 June 2023; published 13 June 2023)

Rapid developments for topological materials have promoted the search for topological transport in the fields of condensed-matter physics and materials science. However, topological network transport, proposed in twisted bilayer graphene and soon after being explored in other two-dimensional materials, is still elusive despite extensive experimental efforts. Here, we implemented on-chip phononic crystal networks based on a network unit cell with six channels consisting of triangular prisms on a silicon substrate arranged in a honeycomb array. The topological network bulk transport in the gap of the bulk states of the original phononic crystal and the network edge transport in the gap of the network bulk states were visualized directly. These results offer a controllable platform for exploring topological transport in networks and may enable the realization of on-chip microultrasonic devices, such as splitters, filters, and signal processing in a monolithic elastic network.

DOI: 10.1103/PhysRevB.107.245122

I. INTRODUCTION

Topological transport that exhibits robust propagation of the edge state is immune to defects and disorders, and is protected by the bulk topology. The discovery of functional topological transport for electronic, electromagnetic, acoustic, and elastic waves is an exciting field, along with the rapid development of topological physics [1–5]. As a well-known paradigm, valley topological insulators, characterized by valley Chern numbers, possess an abundance of valley-related transports [6–12], such as abnormal energy partition [10–12]. For elastic waves, topological transport is of great significance in the fields of nondestructive material testing, high-sensitivity sensing, and information processing [13–19]. Owing to the controllability of sample fabrication and experimental measurements, elastic wave systems provide a flexible platform for exploring topological physics [20–27]. A benefit from the development of micromachining technology, it is possible and intellectually attractive to achieve the sample size of the geometry in the um range for manipulating the elastic wave in megahertz regime [23–27]. This can reach the level of sensing and information processing applications. For instance, topological elastic edge states in a single channel and a four-channel structure formed by two distinct valley phases have been observed in on-chip phononic crystals (PCs) [28,29]. Therefore, it is highly desirable to explore topological transport to design robust and steerable elastic wave devices for topological materials.

Recently, owing to its fascinating electronic behavior, twisted bilayer graphene has garnered considerable interest and shown various unusual phenomena in applications such as unconventional insulators and superconductors [30–32]. In the presence of a perpendicular electric field, twisted bilayer graphene with a tiny twist angle has a band gap and hosts the in-gap network states formed by the valley edge states in the domain wall between the *AB* and *BA* stacking [33–39]. Subsequently, a network of valley topological domain walls with staggered potentials in monolayer graphene was proposed as an alternative way to explore topological network transport [40,41]. In twisted bilayers of graphene, different domains are obtained by stacking and twisting the graphene sheets, which arise from the Moiré pattern. While in the network of valley domain walls, different domains are directly fabricated from the original valley phases. There are two types of network transport: Network bulk states and network edge states [41], which can be attributed to the superlattice effect and cannot emerge in the original lattice.

In the network of valley domain walls, the network bulk and edge states are derived from the edge states between distinctly topological phases in the superlattice, thus they both exist in the bulk band gap of the underlying cell, and transport in the channels of the superlattice network. Especially, the network edge states appear only on the sawtooth boundary while they disappear on the trident boundary, and their distribution on the upper or lower sawtooth boundary is further determined by the connectivity of the superlattice. And the superlattice structure is easier to be adjusted for the needs of different

*These authors contributed equally to this work.
†Corresponding author: dengwy@scut.edu.cn
‡Corresponding author: phjylu@scut.edu.cn
§Corresponding author: phxqhuang@scut.edu.cn
‖Corresponding author: zyliu@whu.edu.cn

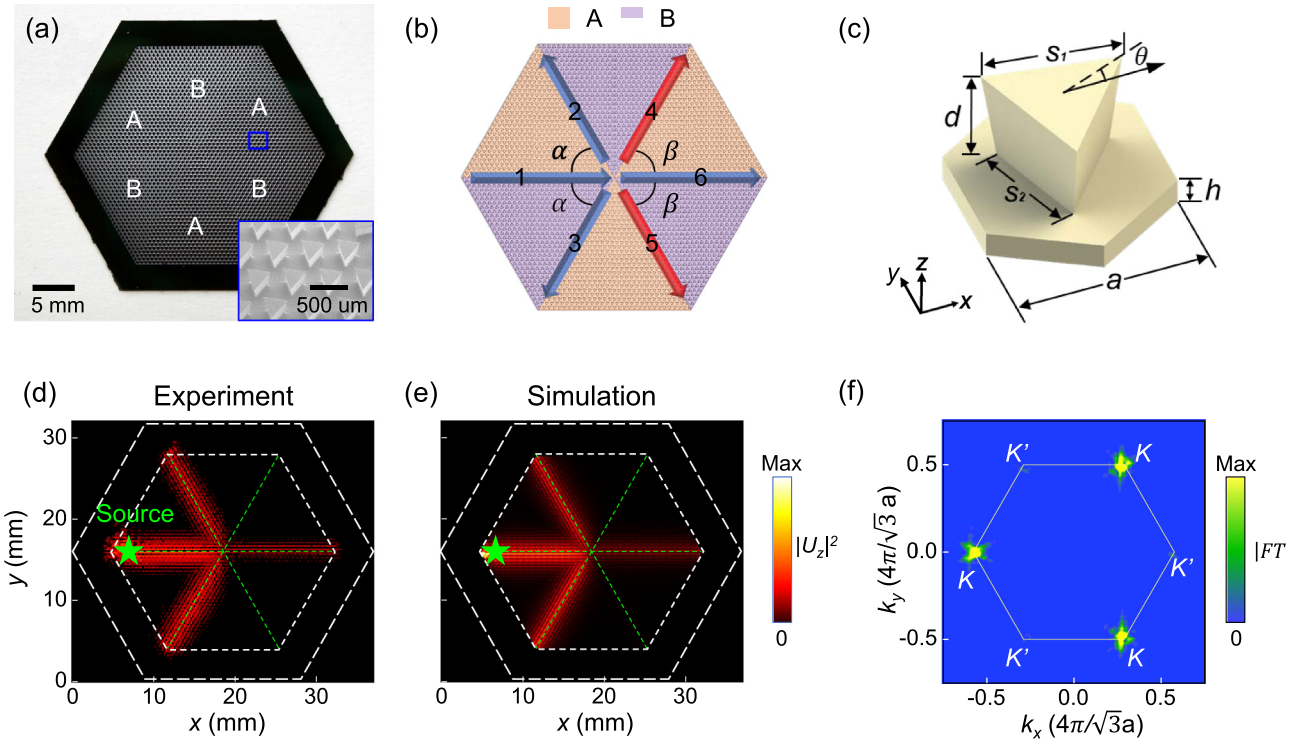

FIG. 1. Topological minimal network transport. (a) Photo of a minimal network with six channels in an on-chip PC, composed of two alternating distinct valley topological PCs, marked A and B. The inset is the scanning electron microscope image, showing an enlarged view of the rectangular area outlined by the blue box. (b) Corresponding schematic of the six channels labeled 1–6 in the minimal network. α and β represent the angles between channels 1 and 2 (or 3), and channels 6 and 4 (or 5), respectively. (c) Schematic side view of the unit cell of PC. The PC is phase A for $0^\circ < \theta < 60^\circ$, and phase B for $-60^\circ < \theta < 0^\circ$. (d), (e) Measured and simulated displacement field intensities of the edge state at a frequency of $f = 1.11$ MHz. The excitation source is marked by the green star. The green dashed lines denote different channels. The white dashed lines represent the inner and outer boundaries of the sample. The PCs are located in the region of the inner hexagon. (f) Fourier spectrum of the measured displacement field illustrated in (d). The white hexagon indicates the first Brillouin zone.

potential applications. Therefore, the network states may provide flexible schemes for field manipulation. However, constructing these topological networks is still a challenge due to the difficulty in atomic-scale engineering [42]. The solid evidence for these unusual network bulk and edge states remains elusive, thus it is desirable to achieve the network states in the elastic platform.

In this study, we realized the networks on an on-chip PC and observed the topological network bulk and edge transports. First, we achieved a minimal topological network with six channels consisting of triangular prisms on a silicon substrate arranged in a honeycomb array. Thereafter, we considered the minimal network as an enlarged network unit cell to construct the network lattice and observe the topological network bulk transport in the bulk gap of the original PC. We further observed the topological network edge transport in the gap between the bands of the network bulk states, which relies on the boundary conditions. All the results, including the topological minimal network transport, topological network bulk, and edge transport, were visualized both in simulations and experiments with good agreement.

II. TOPOLOGICAL MINIMAL NETWORK WITH SIX CHANNELS

We start with the topological minimal network transport with only six channels, which is an enlarged unit cell of the latter network. As shown in Fig. 1(a), a hexagonal sample with six channels was fabricated using deep silicon etching technology. Each channel comprises two distinct topological valley phases, A and B, and all the channels intersect at the center of the hexagonal structure. The corresponding schematics of the six channels labeled as 1–6 are illustrated in Fig. 1(b). The orange and purple colors represent phases A and B, respectively. The angle between channels 1 and 2 (or 3) is α, and that between channels 6 and 4 (or 5) is β. The projected dispersion of a domain wall illustrated in Supplemental Material I [43] indicates that the valley edge states with positive group velocities (blue arrows) in channels 1–3 and 6 are locked with the K valley, whereas those (red arrows) in channels 4 and 5 are locked with the K' valley. When the elastic wave enters from channel 1, owing to negligible intervalley scattering, only channels 2, 3, and 6 are allowed for wave propagation, whereas channels 4 and 5 are prohibited.

The unit cell of phase A was composed of a triangular pillar on top of a silicon plate, which exhibited a positive rotation angle θ with respect to the x axis, as shown in Fig. 1(c). Owing to the fabrication technique, the side surface of the pillar had a trapezoidal shape. The geometric parameters are the lattice constant $a = 500$ μm, the height and side length of the triangular pillars $d = 247$ μm, $s_1 = 350$ μm, and $s_2 = 280$ μm, and the thickness of the bottom plate $h = 72$ μm. Elastic waves on a thin plate, referred to as Lamb waves, are modulated by the

periodic arrangement of pillar scatterers. Positive and negative θ results in different valley topological phases [28]. When $\theta = 0°$, the dispersion hosts the Dirac cones at the K and K' points, which are guaranteed by the C_{3v} symmetry of the unit cell. For other θ, the mirror symmetry along the x direction is broken, which opens a band gap at the Dirac point and gives rise to valley topological phases described by the valley Chern number $C_V = \pm 1/2$. Specifically, for $60° > \theta > 0°$, the valley phase with $C_V = 1/2$ is named phase A; and for $-60° < \theta < 0°$, the valley phase with $C_V = -1/2$ is named phase B. In the following discussion, θ is fixed at $\pm 20°$. Under this condition, a bulk band gap ranging $1.01 - 1.16$ MHz, opens at point K (or K'). By putting the two distinct valley phases together, helical edge states will emerge at the interface and form the channels.

To explore the wave propagation in the six-channel network, the sample with $\alpha = \beta = 60°$ is fabricated, as shown in Fig. 1(a). A needlelike source with a diameter of 5 μm bound on a piezoelectric ceramic is placed at the left entrance of channel 1 to excite the edge states. The detailed sample preparation and experimental methods are discussed in Supplemental Material II [43]. The measured intensity distribution of the z component of the displacement field $|u_z|^2$ at $f = 1.11$ MHz is shown in Fig. 1(d). As expected, the elastic waves were split into channels 2, 3, and 6. Owing to the mirror symmetry of channel 1, the field intensities in channels 2 and 3 remained the same. Interestingly, the field in channel 6 was significantly smaller than those in channels 2 and 3 because the mode coupling between channels 1 and 2 (or 3) is stronger than that between channels 1 and 6 in space. Specifically, the measured transmission of channel 6 was 0.185, whereas those of channels 2 and 3 were 0.407. The corresponding simulated results are shown in Fig. 1(e) and are consistent with the experimental results. By Fourier-transforming the measured field illustrated in Fig. 1(f), only three bright spots were observed at the K points, indicating negligible intervalley scattering. This confirms the robustness of the edge states and that the states in channels 4 and 5 are prohibited. The absorbing materials, that is, the photoresist and silica gel, were coated on the border of the sample (white dotted frame) to avoid reflection waves.

In the above discussion, the field ratio between different channels was fixed for a certain structure. One question that remains unanswered is how to manipulate the specific field distributions in different channels. When $\alpha = 60°$, the configurations of channels 1, 2, 3, and 6 are the same as those illustrated in Fig. 1(d). Because there are no field distributions in channels 4 and 5, it seems that β plays no role to the field distributions in other channels. However, when β was increased from 60° to 90°, the measured field in channel 6 became comparable to those in channels 2 and 3, as shown in Fig. 2(a). In contrast, when β was reduced to 30°, the measured field in channel 6 disappeared. The measured transmission of channel 2 (or 3) was approximately 10 times that of channel 6, as shown in Fig. 2(b). When β was fixed at 60° and α was decreased to 30°, the measured field distributions obtained [Fig. 2(c)] were similar to those illustrated in Fig. 2(b), where the transmissions in channels 2 and 3 are significantly stronger than those in channel 6. The corresponding simulated results [Figs. 2(e)–2(g)] are consistent with the experimental results. Therefore, we can conclude that, although the waves are not allowed to transmit into channels 4 and 5, they play a crucial role in the manipulation of transmissions in other channels. Schematics of the studies on the effect of α and β are illustrated in Figs. 2(d) and 2(h) respectively, where one of them is extended to a range of approximately 15-105° with another angle fixed at 60°. While changing α with β fixed at 60°, the transmission ratio between channel 2 and channel 1 can be roughly fitted using the function $T_{21}(\alpha) = 0.48718 - 6.32432 \times 10^{-5} \times \alpha^2$ and, correspondingly, the transmission ratio between channel 6 and channel

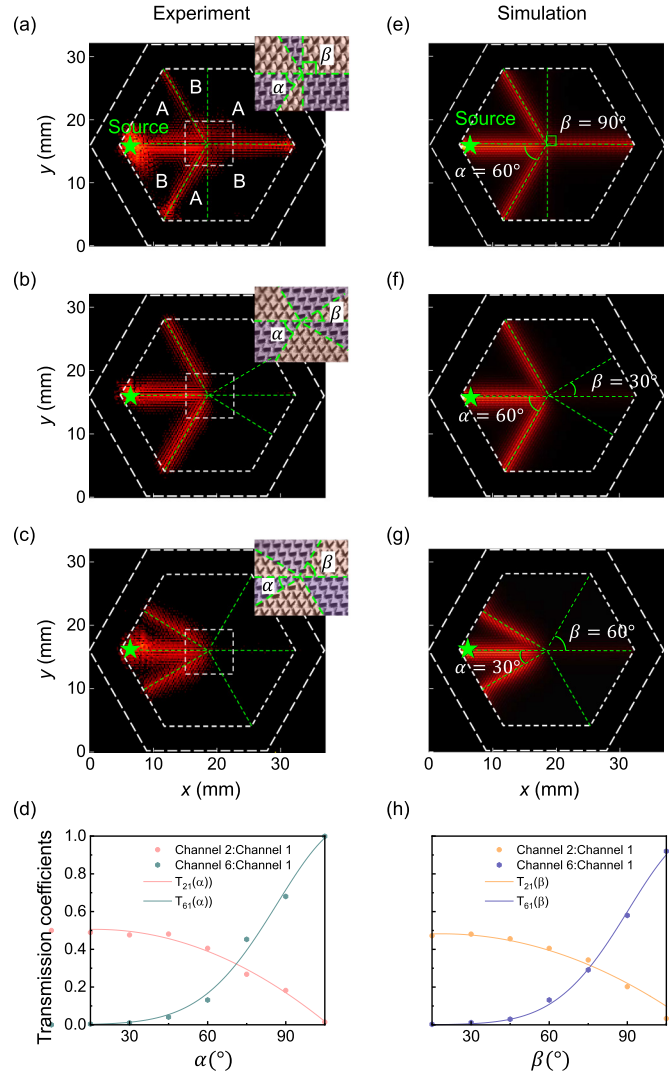

FIG. 2. (a)–(c) Measured intensity distributions of valley edge states with different configurations specified by $\alpha = 60°$, $\beta = 90°$ (a), $\alpha = 60°$, $\beta = 30°$ (b), and $\alpha = 30°$, $\beta = 60°$ (c). Insets: The zoomed-in photos at the intersection, marked by the white dashed boxes. (e)–(g) Simulated intensity distributions of the valley edge state corresponding to (a)–(c). The green stars denote the positions of the point source. (d),(h) Transmission coefficients of channels 2 and 6 compared with channel 1 as a function of orientation angle α with $\beta = 60°$ (d) and β with $\alpha = 60°$ (h), respectively. The dots represent the simulated results and the lines are the empirical curves fit with dots. The operating frequency was set as $f = 1.11$ MHz.

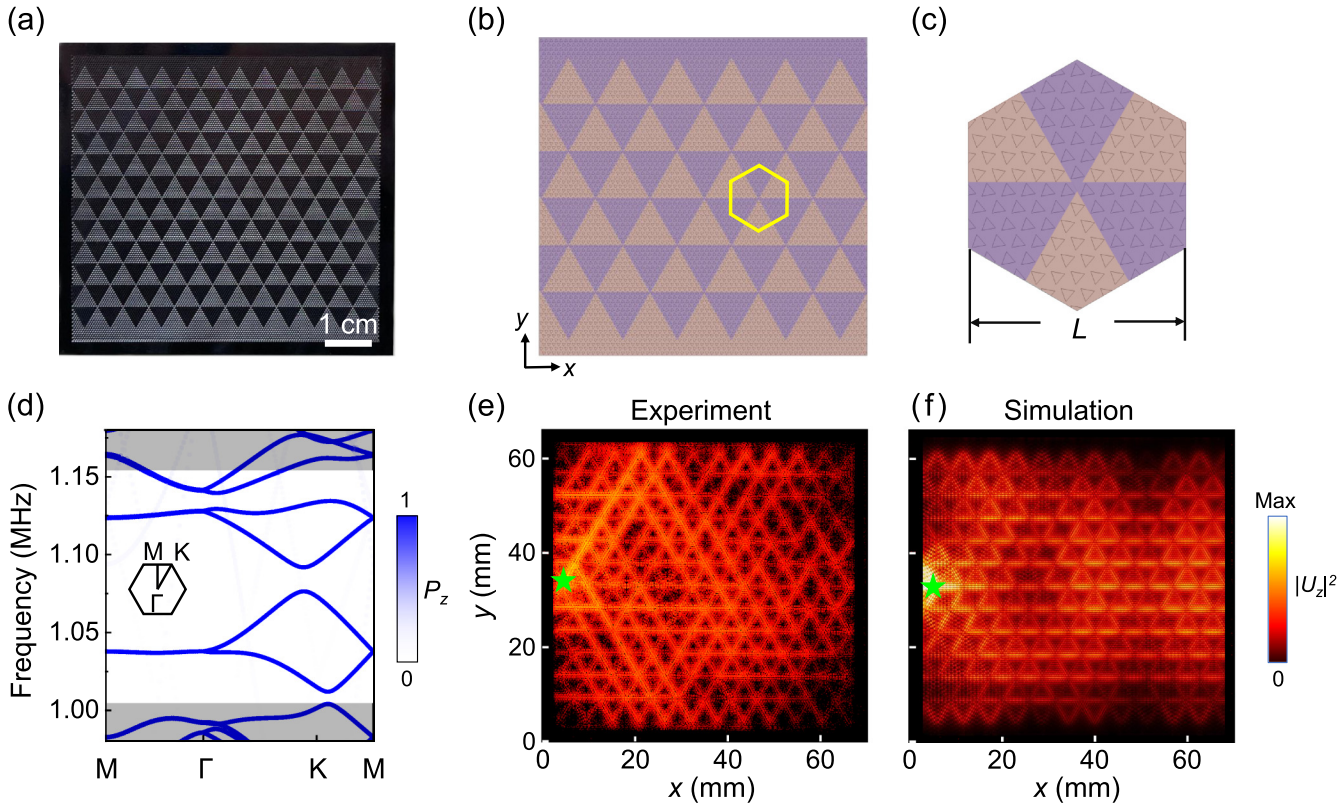

FIG. 3. Topological network bulk transport. (a) Photo of the PC sample of the topological network. (b) Schematic of the topological network of the domain wall channels. The orange and purple regions correspond to the distinct valley PCs in phases A and B, respectively. (c) The network unit cell with six channels is the same as the topological minimal network, corresponding to the yellow hexagon in (b). The lattice constant L is fixed at $11a$. (d) Simulated bulk band dispersion along the high-symmetry lines in the first Brillouin zone of the network. The color indicates the weight of the out-of-plane polarized modes. Gray areas denote the bulk bands of the original valley PC. Inset: The first Brillouin zone for the network unit cell. (e), (f) Measured and simulated field distributions of the network bulk states at a frequency of 1.11 MHz in the topological network, respectively. The green stars denote the positions of the excitation source.

1 can be empirically described by $T_{61}(\alpha) = e^{(-7.889-5.921\alpha^2)}$. Similarly, we can have that $T_{21}(\beta) = 0.4645 - 5.1492 \times 10^{-5} \times \beta^2$ and $T_{61}(\beta) = e^{(-9.21-6.6125\beta^2)}$, for the case where β changes with $\alpha = 60°$. The angles α and β provide a flexible way to tune the partition ratio between different channels. By tuning α and β, the desired transmission in different channels can be realized conveniently.

III. TOPOLOGICAL NETWORK BULK STATES

Based on the minimal network with six channels, we studied the topological network transport in the sample shown in Fig. 3(a) with a size of 66 mm × 63 mm. The PC network of the domain walls was constructed using a superlattice with a hexagonal lattice, as illustrated in Fig. 3(b). The network unit cell with lattice constant L is the reduced minimal network discussed above, as shown in Fig. 3(c), hosting six channels of the domain wall. Figure 3(d) shows the bulk band dispersion along the high-symmetry lines for $L = 11a$, where P_z denotes the ratio of the out-of-plane polarized Lamb waves calculated using $\int_{\text{u.c.}} |u_z|^2 d\boldsymbol{r} / \int_{\text{u.c.}} |\boldsymbol{u}|^2 d\boldsymbol{r}$ in the network unit cell. It is evident that four bands with the states dominated by the out-of-plane polarization appear in the bulk band gap of the original valley PC illustrated in Fig. 1(c), ranging 1.01–1.16 MHz (between the gray areas). These states are confined to the channels of the domain walls in the network unit cell and are thus the topological network bulk states. They are protected by the valley topology and robust against weak disorders and defects, similar to the edge states at the interface between these two distinct valley phases. To excite the network bulk state, a point source was placed at the middle of the left boundary at a frequency of 1.11 MHz. As shown in Fig. 3(e), the measured field diffuses throughout the sample, which is consistent with the simulated results illustrated in Fig. 3(f). The configurations of the network bulk bands and the localizations of the network bulk states can be tuned by the lattice constant L, as discussed in Supplemental Material III [43].

IV. TOPOLOGICAL NETWORK EDGE STATES

We then explored the boundary effect of the PC network and determined the topological network edge states along the x direction. As shown in Fig. 3(b), two types of boundaries, the sawtooth and trident boundaries, exist along the x and y directions, respectively. The projected band dispersion of the network ribbon, with a periodic boundary along the x direction and an open boundary along the y direction, is shown in Fig. 4(a). Network edge states exist in the gaps of the network bulk states (white circles), as indicated by

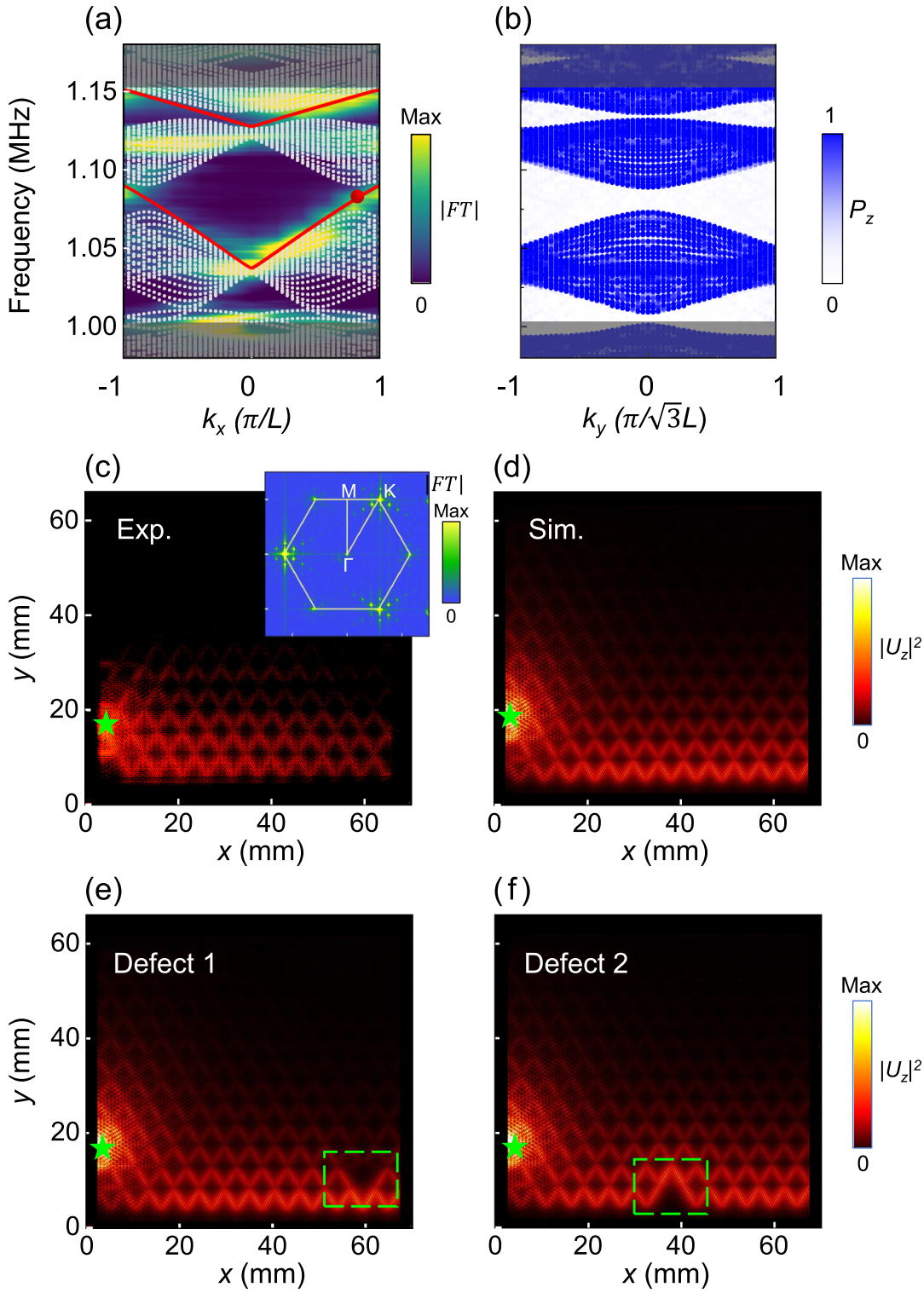

FIG. 4. Topological network edge transport. (a) Projected band dispersions along the k_x directions. Color maps represent the measured data. The white circles mainly denote the simulated network bulk states, and the red lines represent the simulated network edge states. The gray areas denote the bulk bands of the original valley PC. (b) Simulated projected band dispersions along the k_y directions. No network edge states are observed in the band gaps of the network bulk states (blue circles). (c), (d) Measured and simulated field distributions of the network edge states [red sphere in (a)] in the topological network, respectively. Inset in (c): the corresponding Fourier spectrum of the measured displacement field. (e), (f) Simulated field distributions of the network edge states in the presence of defects at two different positions (the green dashed rectangles). The operating frequency is set at 1.08 MHz, and the green stars denote the positions of the excitation source.

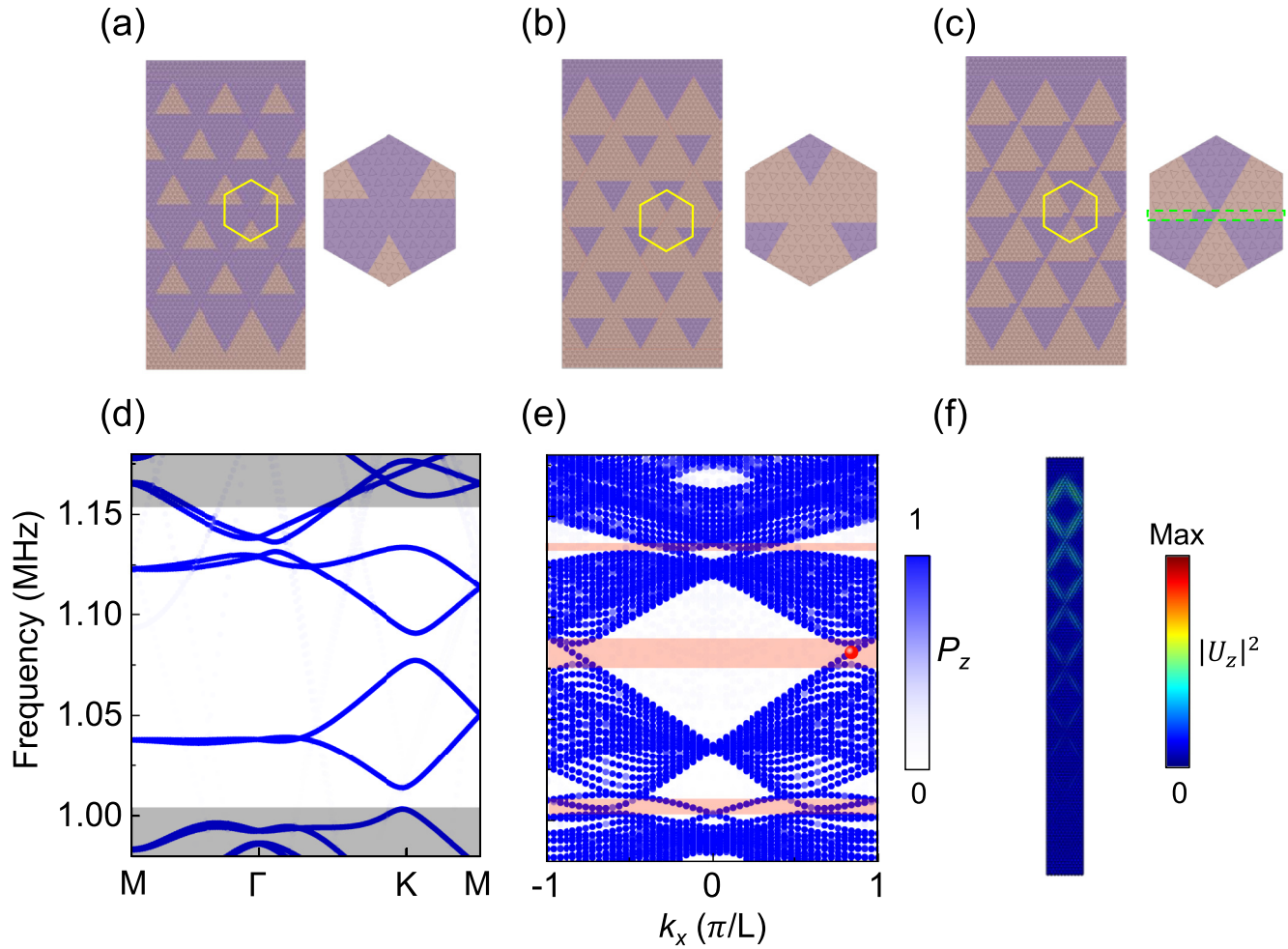

FIG. 5. (a)–(c) Schematic of three topological networks with different filling ratios of PCs in phases A and B. (d) Simulated bulk band structure along the high-symmetry lines in the first Brillouin zone of the network in (c). (e) Simulated projected band dispersions along the k_x directions. (f) Eigenfield distribution of the edge state [red sphere in (e)] at a frequency of 1.08 MHz.

the red lines, which can be attributed to the valley topology of the network bulk states and boundary conditions of the ribbon [41]. In the experimental sample, six layers of cladding were added at the upper and lower boundaries to fill the absorbing material, which did not change the dispersion of the network edge states, as shown in Supplemental Material IV [43]. The experimental result was obtained through Fourier transformation of the displacement fields, as illustrated by the color map, which agrees well with the simulated result. The network edge states of the network unit cell shown in Fig. 3(c) existed only at the lower edge and vanished at the upper edge of the x-direction boundary. Figure 4(b) shows the projected band dispersion of the network ribbon with an open boundary along the x direction. No network edge states were observed in the band gaps of the network bulk states for either the left or right edges of the y-direction boundaries.

We further demonstrate the robustness of network edge transport. The measured and simulated field distributions at a frequency of 1.08 MHz in the middle band gap of the network bulk states are shown in Figs. 4(e) and 4(f), respectively, verifying the existence of network edge states at the lower edge of the x-direction boundary. A point source (green star) at the left boundary was used to stimulate the elastic waves in the experiment. From the Fourier transformation of the measured field, it is evident that the network edge states are mainly located at the K valley when transported along the positive direction, thus maintaining the valley-momentum locking property. Therefore, the network edge states are topological and robust against bending and defects. Figures 4(e) and 4(f) show the field distributions of the network edge states in the presence of defects at two different positions, where the defects were generated by digging out the network unit cells. It was observed that the network edge states could still propagate from the left side to the right side without changing the strength, confirming topological network edge transport. In addition, the network edge state is stable and unaffected by the theta of scatterer arrays in the selected unit cell, as discussed in Supplemental Material V [43].

A puzzling question arises: Why are there no edge states at the upper edge of the x-direction boundary? To analyze this problem, we first considered two special cases: the filling ratio of the PC with phase A in a unit cell is significantly less than that with phase B, and the second case is the opposite. The first case is shown in the schematic of the network illustrated in Fig. 5(a). PCs in phase A became isolated regions surrounded by those in phase B, except for the lower boundary.

Therefore, the discontinuity of the domain wall at the upper boundary resulted in the absence of edge states. In contrast, for the second case, as shown in Fig. 5(b), the discontinuity of the domain wall occurred at the lower boundary, resulting in the absence of edge states. Between them, a transition occurs for a certain filling ratio of PC with phase A (or phase B). The configuration in Fig. 3(c) demonstrates one more row of phase B than phase A, as marked by the green dashed box, where the edge states are confined to the lower edge. By decreasing the filling ratio of phase B to the structure in Fig. 5(c), the bulk band structure and associated projected band dispersion were determined, as shown in Figs. 5(d) and 5(e), respectively. In contrast, the field distribution of the edge state [red sphere in Fig. 5(e)] was localized at the upper edge rather than at the lower edge, as shown in Fig. 5(f). Therefore, the edge states can be modulated by varying the filling ratio of phase A (or phase B). The underlying physics of this transition is attributed to the closing of the middle band gap. The bulk band structure as a function of the filling ratio of phase A is shown in Supplemental Material VI [43].

V. SUMMARY

In conclusion, we have realized elastic topological network transport in on-chip PCs using silicon-based microfabrication. Both topological network bulk and network edge states were visualized directly. A network unit cell with six channels can be used as an elastic wave splitter in which the input elastic wave is only divided into the forward channel and two other channels adjacent to the incident channel, and the energy partition can be modulated by tuning the geometry angles between different channels. The topological bulk and edge transports are attributed to the superlattice effect and provide schemes for controlling elastic waves. These on-chip topological network transports can be applied to microelectromechanical systems and are available in acoustic arithmetic and logical units that can be integrated with ultrasonic waveguide devices.

ACKNOWLEDGMENTS

This work was supported by the National Key R&D Program of China (Grants No. 2022YFA1404500, No. 2022YFA1404900, and No. 2018YFA0305800), National Natural Science Foundation of China (Grants No. 11890701, No. 11974120, No. 11974005, No. 12074128, No. 12222405, and No. 12204290), and Guangdong Basic and Applied Basic Research Foundation (Grants No. 2019B151502012, No. 2021B1515020086, No. 2021A1515110812, and No. 2022B1515020102).

[1] S. Das Sarma, S. Adam, E. H. Hwang, and E. Rossi, Rev. Mod. Phys. **83**, 407 (2011).
[2] X. L. Qi and S. C. Zhang, Rev. Mod. Phys. **83**, 1057 (2011).
[3] M. Z. Hasan, G. Chang, I. Belopolski, G. Bian, S. Y. Xu, and J. X. Yin, Nat. Rev. Mater. **6**, 784 (2021).
[4] T. Ozawa, H. M. Price, A. Amo, N. Goldman, M. Hafezi, L. Lu, M. C. Rechtsman, D. Schuster, J. Simon, O. Zilberberg, and I. Carusotto, Rev. Mod. Phys. **91**, 015006 (2019).
[5] G. Ma, M. Xiao, and C. T. Chan, Nat. Rev. Phys. **1**, 281 (2019).
[6] L. Ju, Z. Shi, N. Nair, Y. Lv, C. Jin, J. V. Jr., C. Ojeda-Aristizabal, H. A. Bechtel, M. C. Martin, A. Zettl, J. Analytis, and F. Wang, Nature (London) **520**, 650 (2015).
[7] J. R. Schaibley, H. Yu, G. Clark, P. Rivera, J. S. Ross, K. L. Seyler, W. Yao, and X. Xu, Nat. Rev. Mater. **1**, 16055 (2016).
[8] F. Zhang, A. H. MacDonald, and E. J. Mele, Proc. Natl. Acad. Sci. USA **110**, 10546 (2013).
[9] J. Li, K. Wang, K. J. McFaul, Z. Zern, Y. Ren, K. Watanabe, T. Taniguchi, Z. Qiao, and J. Zhu, Nat. Nanotechnol. **11**, 1060 (2016).
[10] F. Gao, H. Xue, Z. Yang, K. Lai, Y. Yu, X. Lin, Y. Chong, G. Shvets, and B. Zhang, Nat. Phys. **14**, 140 (2018).
[11] Z. Qiao, J. Jung, C. Lin, Y. Ren, A. H. MacDonald, and Q. Niu, Phys. Rev. Lett. **112**, 206601 (2014).
[12] J. Li, R.-X. Zhang, Z. Yin, J. Zhang, K. Watanabe, T. Taniguchi, C. Liu, and J. Zhu, Science **362**, 1149 (2018).
[13] M. Miniaci and R. K. Pal, J. Appl. Phys. **130**, 141101 (2021).
[14] X. Ding, P. Li S.-C. S. Lin, Z. S. Stratton, N. Nama, F. Guo, D. Slotcavage, X. Mao, J. Shi, F. Costanzoa, and T. J. Huang, Lab Chip **13**, 3626 (2013).
[15] Y. Q. Fu, J. K. Luo, N. T. Nguyen, A. J. Walton, A. J. Flewitt, X. T. Zu, Y. Li, G. McHale, A. Matthews, E. Iborra, H. Du, and W. I. Milne, Prog. Mater. Sci. **89**, 31 (2017).
[16] D. Hatanaka, I. Mahboob, K. Onomitsu, and H. Yamaguchi, Nat. Nanotechnol. **9**, 520 (2014).
[17] B. J. Ash, S. R. Worsfold, P. Vukusic, and G. R. Nash, Nat. Commun. **8**, 174 (2017).
[18] J. Cha and C. Daraio, Nat. Nanotechnol. **13**, 1016 (2018).
[19] J. Qi, Z. Chen, P. Jiang, W. Hu, Y. Wang, Z. Zhao, X. Cao, S. Zhang, R. Tao, Y. Li, and D. Fang, Adv. Sci. **9**, 2102662 (2022).
[20] P. Wang, L. Lu, and K. Bertoldi, Phys. Rev. Lett. **115**, 104302 (2015).
[21] S. H. Mousavi, A. B. Khanikaev, and Z. Wang, Nat. Commun. **6**, 8682 (2015).
[22] S. Y. Yu, C. He, Z. Wang, F. Liu, X. Sun, Z. Li, H. Lu, M. Lu, X. Liu, and Y. Chen, Nat. Commun. **9**, 3072 (2018).
[23] M. Miniaci, R. K. Pal, B. Morvan, and M. Ruzzene, Phys. Rev. X **8**, 031074 (2018).
[24] J. Cha, K. W. Kim, and C. Daraio, Nature (London) **564**, 229 (2018).
[25] M. Miniaci, R. K. Pal, R. Manna, and M. Ruzzene, Phys. Rev. B **100**, 024304 (2019).
[26] M. P. Makwana and G. Chaplain, Sci. Rep. **9**, 18939 (2019).
[27] G. Yu, W. Wang, L. Lai, T. Peng, C. Jiang, and Y. Li, Int. J. Mech. Sci. **241**, 107989 (2023).
[28] M. Yan, J. Lu, F. Li, W. Deng, X. Huang, J. Ma, and Z. Liu, Nat. Mater. **17**, 993 (2018).
[29] Q. Zhang, D. Lee, L. Zheng, X. Ma, S. I. Meyer, L. He, H. Ye, Z. Gong, B. Zhen, Lai K, and A. T. Charlie Johnson, Nat. Electron. **5**, 157 (2022).
[30] Y. Cao, V. Fatemi, A. Demir, S. Fang, S. L. Tomarken, J. Y. Luo, J. D. Sanchez-Yamagishi, K. Watanabe, T. Taniguchi, E. Kaxiras, R. C. Ashoori, and P. Jarillo-Herrero, Nature (London) **556**, 80 (2018).

[31] Y. Cao, V. Fatemi, S. Fang, K. Watanabe, T. Taniguchi, E. Kaxiras, and P. Jarillo-Herrero, Nature (London) **556**, 43 (2018).

[32] X. Lu, P. Stepanov, W. Yang, M. Xie, M. A. Aamir, I. Das, C. Urgell, K. Watanabe, T. Taniguchi, G. Zhang, A. Bachtold, A. H. MacDonald, and D. K. Efetov, Nature (London) **574**, 653 (2019).

[33] S. Huang, K. Kim, D. K. Efimkin, T. Lovorn, T. Taniguchi, K. Watanabe, A. H. MacDonald, E. Tutuc, and B. J. LeRoy, Phys. Rev. Lett. **121**, 037702 (2018).

[34] P. Rickhaus, J. Wallbank, S. Slizovskiy, R. Pisoni, H. Overweg, Y. Lee, M. Eich, M. Liu, K. Watanabe, T. Taniguchi, T. Ihn, and K. Ensslin, Nano Lett. **18**, 6725 (2018).

[35] H. Yoo, R. Engelke, S. Carr, S. Fang, K. Zhang, P. Cazeaux, S. H. Sung, R. Hovden, A. W. Tsen, T. Taniguchi, K. Watanabe, G. C. Yi, M. Kim, M. Luskin, E. B. Tadmor, E. Kaxiras, and P. Kim, Nat. Mater. **18**, 448 (2019).

[36] S. G. Xu, A. I. Berdyugin, P. Kumaravadivel, F. Guinea, R. K. Kumar, D. A. Bandurin, S. V. Morozov, W. Kuang, B. Tsim, S. Liu, J. H. Edgar, I. V. Grigorieva, V. I. Fal'ko, M. Kim, and A. K. Geim, Nat. Commun. **10**, 4008 (2019).

[37] C. De Beule, F. Dominguez, and P. Recher, Phys. Rev. Lett. **125**, 096402 (2020).

[38] P. San-Jose and E. Prada, Phys. Rev. B **88**, 121408(R) (2013).

[39] D. K. Efimkin and A. H. MacDonald, Phys. Rev. B **98**, 035404 (2018).

[40] T. Hou, Y. Ren, Y. Quan, J. Jung, W. Ren, and Z. Qiao, Phys. Rev. B **102**, 085433 (2020).

[41] T. Hou, Y. Ren, Y. Quan, J. Jung, W. Ren, and Z. Qiao, Phys. Rev. B **101**, 201403(R) (2020).

[42] A. Jorio, Nat. Mater. **21**, 844 (2022).

[43] See Supplemental Material at http://link.aps.org/supplemental/10.1103/PhysRevB.107.245122 for the bulk band dispersion and projected band dispersion of the original PC (I); sample preparation and experimental platform construction (II); influence of the size of the network unit cell (III); the claddings of the network sample in experiment (IV); influence of the θ in the network unit cell (V); and the bulk band structures for different filling ratios of phase A (VI).